Evidence of Changes of Seismic Properties in the Entire Crust Beneath Japan After the M w 9.0, 2011 Tohoku-oki Earthquake

Qing-Yu Wang, Michel Campillo, Florent Brenguier, Albanne Lecointre, Tetsuya Takeda, Akinori Hashima

JGR Solid Earth

RESEARCH ARTICLE
10.1029/2019JB017803

Evidence of Changes of Seismic Properties in the Entire Crust Beneath Japan After the M_w 9.0, 2011 Tohoku-oki Earthquake

Qing-Yu Wang[1], Michel Campillo[1], Florent Brenguier[1], Albanne Lecointre[1], Tetsuya Takeda[2], and Akinori Hashima[3]

[1]Université Grenoble Alpes, CNRS, ISTerre, Grenoble, France, [2]National Research Institute for Earth Science and Disaster Resilience, Tsukuba, Japan, [3]Earthquake Research Institute, University of Tokyo, Tokyo, Japan

Key Points:
- We measure seismic waves velocity changes in the period range of 1–50 s
- Monitoring results show both dynamic and static strain-related seismic velocity changes
- There are delayed seismic responses to the Tohoku-oki earthquake from the lower crust

Correspondence to:
Q.-Y. Wang,
qingyu.wang@univ-grenoble-alpes.fr

Citation:
Wang, Q.-Y., Campillo, M., Brenguier, F., Lecointre, A., Takeda, T., & Hashima, A. (2019). Evidence of changes of seismic properties in the entire crust beneath Japan after the M_w 9.0, 2011 Tohoku-oki earthquake. *Journal of Geophysical Research: Solid Earth*, *124*, 8924–8941. https://doi.org/10.1029/2019JB017803

Received 9 APR 2019
Accepted 6 AUG 2019
Accepted article online 13 AUG 2019
Published online 24 AUG 2019

Abstract Studies of mechanical responses of the Earth crust to large earthquakes can provide us with unique insights into the processes of stress buildup and release. As a complement to geodetic methods that derive crustal strain dynamics from surface observations (e.g., GPS, InSAR), noise-based seismic velocity monitoring directly probes the mechanical state of the crust, at depth and continuously in time. We investigate the responses of the crust to the M_w 9.0, 2011 Tohoku-oki earthquake. In addition to the Hi-net short-period sensors, we use Hi-net tiltmeters as long-period seismometers (8–50 s) to sample the crust below 5 km in depth. The spatial distribution of the strong velocity decreases at short periods appears to be limited to the region of strong ground shaking induced by the 2011 Tohoku-oki earthquake, while the long-period velocity changes correlate well with the modeled static strain induced by viscoelastic relaxation and afterslip at depth. Amplitudes of coseismic velocity changes decrease with increasing depth. The temporal evolution of velocity changes in different period bands shows that the maximum drops in the velocity at long periods are delayed in time with respect to the occurrence of the Tohoku-oki earthquake. The inversion of seismic velocity changes at depth illustrates how *S* wave velocities evolve down to 40 km at a regional scale after a major earthquake.

1. Introduction

Stress changes and relaxation following earthquakes produce postseismic processes. The study of postseismic processes is crucial to an understanding of the local rheology of the crust and earthquake interactions (Bürgmann & Dresen, 2008; Freed et al., 2006, 2007; Fukushima et al., 2018; Pollitz, 1992, 2005). Over the past 10 years, noise-based seismic monitoring has started to be used for observations of near-surface damage induced by large earthquakes (Brenguier, Campillo, et al., 2008; Taira et al., 2015; Wegler & Sens-Schönfelder, 2007; Wegler et al., 2009). The continuous monitoring of seismic velocities offers a new tool to capture the physical processes that take place after large earthquakes. This can provide insights not only into the tectonic and volcanic processes (Brenguier, Campillo, et al., 2008; Brenguier, Shapiro, et al., 2008; Brenguier et al., 2014; Chen et al., 2010; Froment et al., 2013; Obermann et al., 2013; Taira & Brenguier, 2016; Wegler et al., 2009) but also into some transient fluctuations that are derived from external environmental perturbations (Sens-Schönfelder & Wegler, 2006; Meier et al., 2010; Hillers et al., 2014; Hillers, Ben-Zion, et al., 2015; Wang et al., 2017). The characteristic depth at which such changes can be monitored varies from meters (Hillers, Retailleau, et al., 2015; Mao et al., 2019; Sens-Schönfelder & Wegler, 2006) down to dozens of kilometers into the crust (Froment et al., 2013; Obermann et al., 2014; Rivet et al., 2013), through measurements at various periods. Our goal here is to investigate changes down to 40 km in depth at a regional scale after a significant earthquake.

Previous noise-based seismic monitoring studies of the M_w 9.0, 2011 Tohoku-oki earthquake focused on relatively short periods of <10 s, and thus at shallow depths, such as Brenguier et al. (2014), Sawazaki et al. (2015), Gassenmeier et al. (2016), and Wang et al. (2017). Brenguier et al. (2014) and Wang et al. (2017) showed that there is a fast coseismic decrease in velocity followed by long-term exponential postseismic relaxation. Brenguier et al. (2014) indicated that at shallow depth, coseismic velocity drops were mostly induced by shaking from seismic waves emitted by the M_w 9.0 mainshock. The depth of the velocity changes

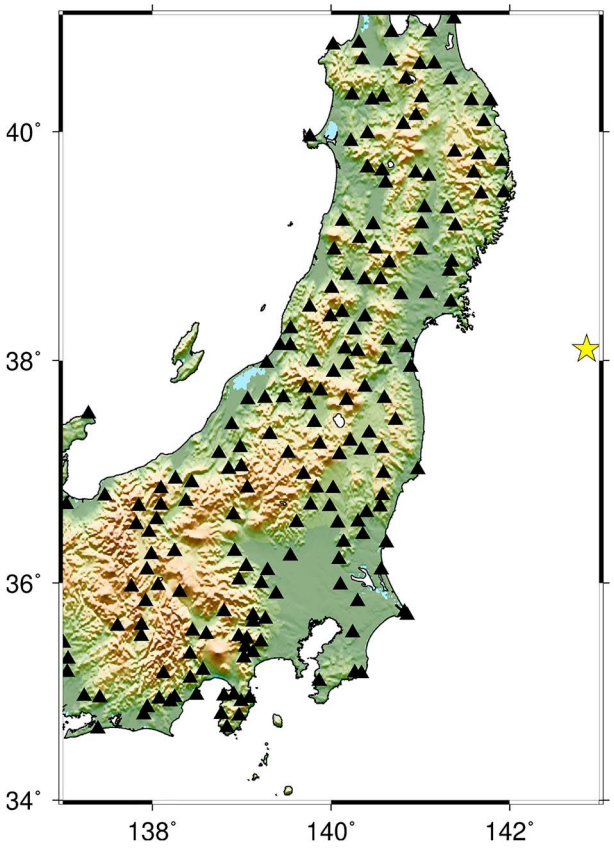

Figure 1. Map of the study area in northeast Honshu. Black triangles indicate the distribution of the 190 selected Hi-net tiltmeter stations; the yellow star shows the epicenter of the M_w 9.0 Tohoku-oki earthquake.

can be estimated by considering the surface wave sensitivity kernels in the upper crust. Minato et al. (2012) showed that earthquake-related seismic velocity changes in the period range of 2 to 10 s contain information from both stress release and strong ground motion at shallow depth. These results show, however, that seismic velocity changes at relatively high frequencies are mostly sensitive to earthquake-related nonlinear responses in the shallow layers (Brenguier et al., 2014; Gassenmeier et al., 2016).

At long periods of 12 to 30 s, Froment et al. (2013) first claimed that seismic velocity changes induced by the M_w 8.0 Wenchuan earthquake were very different from the velocity changes at short periods. Recently, Obermann et al. (2018) constrained this anomaly to 20 to 30 km in depth. The present study was intended to investigate seismic velocity variations induced by the Tohoku-oki earthquake using long-period seismic data (>10 s). We use both Hi-net short-period and tiltmeter data (Obara et al., 2005; Okada et al., 2004) to measure the frequency-dependent velocity changes before, during, and after the M_w 9.0, 2011 Tohoku-oki earthquake. We validate the feasibility of using tiltmeter recordings to measure monthly seismic velocity changes at long periods up to 50 s and combine these observations with results from the Hi-net short-period data corrected for seasonal effects in the period band of 1 to 7 s.

We find that the spatial distribution of the velocity changes shows high correlation with the strong-motion amplitude in the period band of 1 to 7 s and with coseismic dilatation for longer periods of 8 to 30 s. For the long periods, the maximum velocity drop is delayed from the time of the earthquake occurrence with a time lag that depends on the period, which can be as long as 6 months. This phenomenon suggests that the processes at the surface that are responsible for the velocity changes are different from those at depth.

2. Data and Methods

In this study, we restrict the studied area to close to the rupture zone in Honshu. We select 190 tiltmeter stations (Figure 1) with recording gaps of <5% that span from 2008 to 2012. Tonegawa et al. (2006) and Nishida et al. (2008) used tiltmeters as broadband seismometers for receiver function analysis and tomography in Japan, respectively. The comparison of both velocity waveforms and amplitude spectra between recordings from tiltmeters and from nearby broadband stations show strong similarities between these two types of data (Tonegawa et al., 2006).

The routine preprocessing of continuous signals consists of spectral whitening from 0.02 to 0.125 Hz and 1-bit normalization. These operations are aimed at decreasing the effects of temporal changes in the microseismic sources and improving the temporal stability of the noise records (Campillo & Paul, 2003; Shapiro & Campillo, 2004). We smooth the daily cross-correlation functions using a 30-day moving average window and stack the daily functions over every 30 days, starting from 28 January 2008. Then we adopt the doublet and inversion methods of Brenguier et al. (2014) to retrieve accurate monthly velocity changes for all of the 7,636 horizontal component pairs up to 90 km apart. Figure 2a shows 1,000 correlation functions randomly selected from the 7,636 component pairs plotted as a function of the interdistance of pairs. Each of them is randomly chosen within the time period from 2008 to 2012. We see the waveform of direct arrivals waves and coda waves. Figure 2b shows an example of component pair FSWH.N and MGMH.E. We can identify from Figure 2c that the energy continues to decay till ±400 s. After that, the downdip tends to be flat and the signal is dominated by random fluctuation. We measure velocity changes in two-period bands of 8 to 30 s, and 15 to 50 s, for which the moving window lengths are 30 and 50 s, respectively, from −400 to 400 s of the time lag with 60% overlap. For each station, we average all of the related pairs within 90 km and obtain time series of the monthly seismic velocity changes over 5 years. It requires longer time to stabilize the cross-correlation functions for large-period bands; thus, we get lower temporal resolution compared to the results from Hi-net short-period band (Wang et al., 2017).

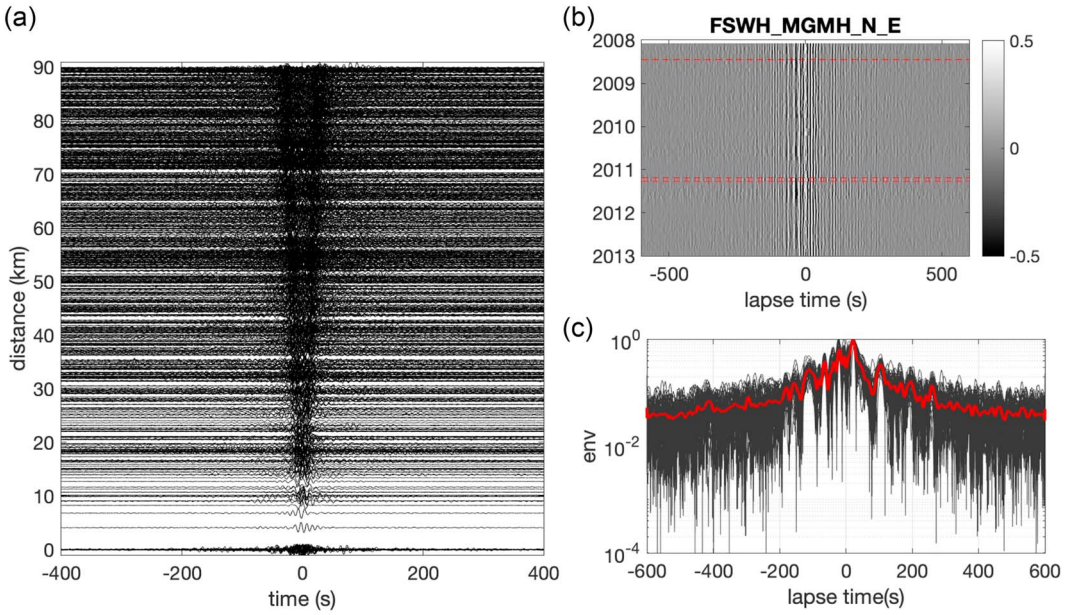

Figure 2. (a) Time-distance plot of correlation functions of 1,000 component pairs. (b) Monthly cross correlation of components FSWH.N and MGMH.E. The three horizontal red dashed lines indicate separately the days of the Iwate-Miyagi Nairiku earthquake, the Tohoku-oki earthquake, and the biggest aftershock. (c) The Hilbert envelop of the cross correlation of components FSWH.N and MGMH.E at different time from 2008 to 2012. Red curve represents the averaged envelop.

3. Spatial and Temporal Evolution of the Seismic Velocity Changes

In addition to measurements using tiltmeter signals for the period of 8 to 50 s, we also measure time series of seismic velocity changes in the period band of 1 to 7 s using both vertical and horizontal components of the Hi-net short-period data, with the same approach that includes the same time average of the cross correlations. Therefore, the smoothness of the responses has exactly the same effects. Furthermore, in the period band of 1 to 7 s, velocity variations are corrected from seasonal effects following the procedures of Wang et al. (2017). The evolution of spatial and temporal seismic velocity changes at different periods allows depth-dependent Tohoku-oki earthquake-related coseismic and postseismic physical processes to be revealed.

We select seven seismic stations at different distances from the epicenter of the Tohoku-oki earthquake to illustrate how the seismic velocity changes in the three different period bands (1–7, 8–30, and 15–50 s). Figure 3a indicates the locations of the seven stations, and Figures 3b–3h show the time series of the seismic velocity changes in the three different period ranges. For each station, the seismic velocity changes are the average over all station pairs within 90 km.

Globally, we observe that the amplitudes of the seismic velocity changes decrease as the period increases. This suggests that the velocities change significantly in the shallow layers and then weaken as the depth increases. However, the ratio of the amplitude within the three time series differs a lot at different locations, as do the postseismic recovery processes, which are very different across the three period bands.

For the short-period band of 1 to 7 s, the coseismic velocity drop is large in proximity to the epicenters. We identify three velocity drops that are coincident with the M_w 6.9, 2008 Iwate-Miyagi Nairiku earthquake, M_w 9, 2011 Tohoku-Oki earthquake, and the M_w 7.1 aftershock of Tohoku-oki earthquake on 7 April 2011. The largest velocity drop occurs at the time of the big aftershock. The 2008 Iwate earthquake-related velocity drops (~0.02%) are seen for stations HMNH and KAKH, near to the epicenter. The 2011 Tohoku-oki earthquake-related large seismic velocity changes ($\sim -0.08\%$) can be clearly observed at all of the seven stations (Figures 3b–3h). The velocities start to recover immediately after the earthquake. Note that the velocity related to the Iwate earthquake does not recover entirely before the occurrence of the Tohoku-oki earthquake, neither do the velocity changes associated with the Tohoku-oki earthquake at the end of 2012.

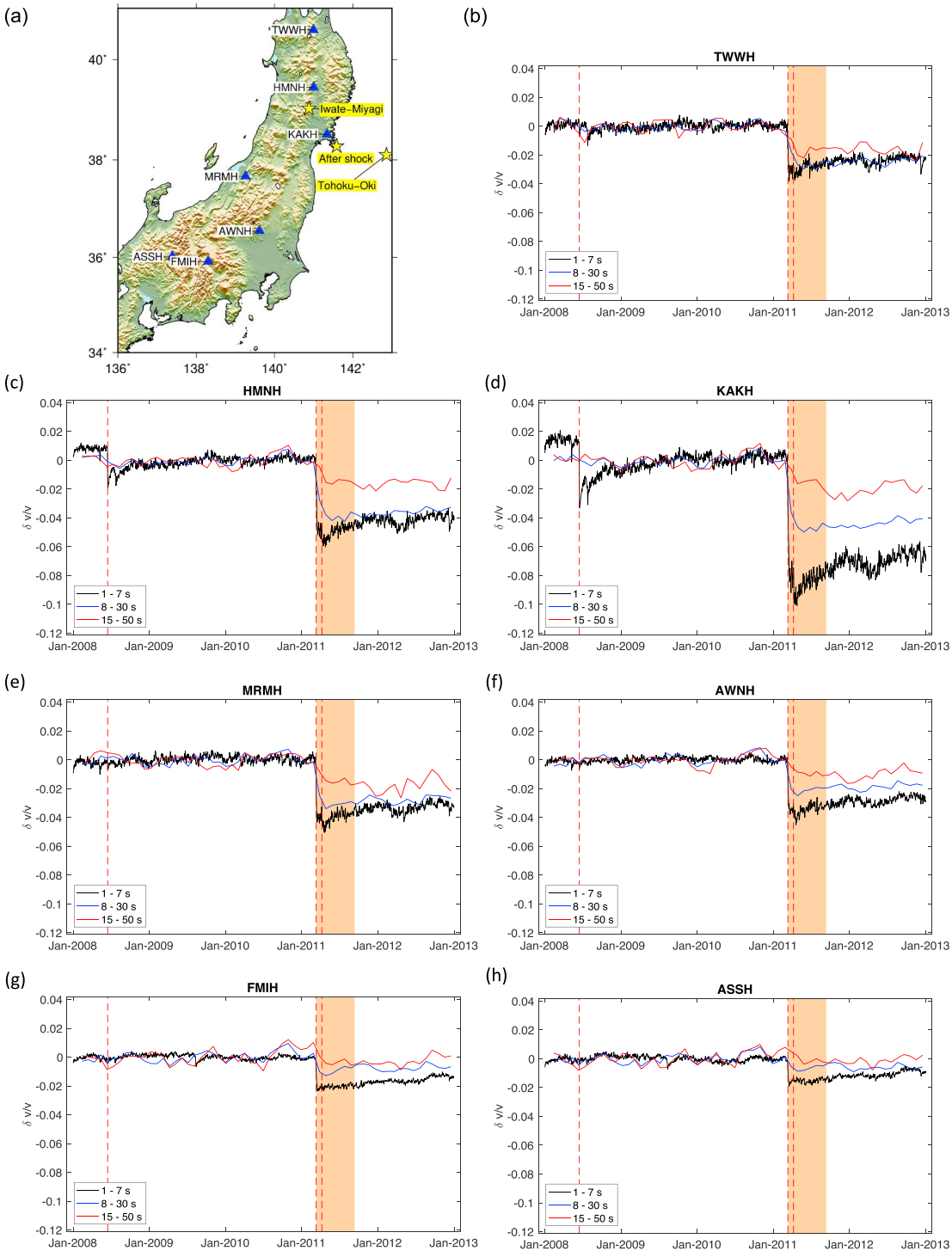

Figure 3. (a) Locations of the seven Hi-net stations. (b–h) Time series of the seismic velocity changes for the different period ranges (1–7, 8–30, and 15–50 s) for the Hi-net stations TWWH, HMNH, KAKH, MRMH, AWNH, FMIH, and ASSH, respectively, from north to south. Yellow stars indicate separately the M_w 6.9, 2008 Iwate-Miyagi Nairiku earthquake (39.030°N 140.881°E), the M_w 9, 2011 Tohoku-Oki earthquake (38.297°N 142.373°E), and the aftershock of Tohoku-oki earthquake (38.1°N 141.86°E). The shaded area includes 6 months after the Tohoku-oki earthquake. The three vertical red dashed lines indicate separately the days of the Iwate-Miyagi Nairiku earthquake, the Tohoku-oki earthquake, and the aftershocks on 7 April 2011.

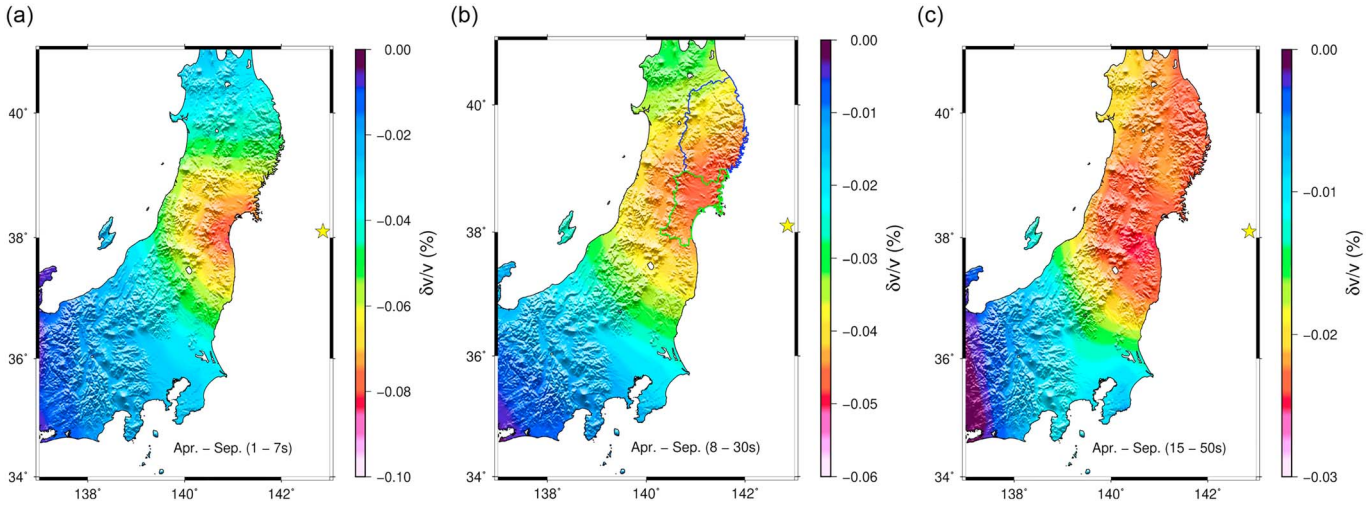

Figure 4. Mapping of the mean coseismic and postseismic velocity changes over the months from April to September, 2011, for the periods of (a) 1 to 7 s, (b) 8 to 30 s, and (c) 15 to 50 s. Blue line and green line in (b) separately outline the border of Iwate prefecture and Miyagi prefecture.

For seismic velocity changes in the relatively long-period bands of 8 to 30 s and 15 to 50 s, the coseismic velocity drops are weaker. We observe unambiguous coseismic velocity drops solely coincident with the 2011 Tohoku-oki earthquake, for stations TWWH, HMNH, KAKH, MRMH, and AWNH. The absolute amplitudes are smaller than that in 1- to 7-s period band. The coseismic and postseismic responses do not differ a lot at different locations. During the first several months after the earthquake, the seismic velocities continue to decrease. The velocities tend to be minimum until around the end of 2011, especially in the period band of 15 to 50 s. This delayed response in time might be controlled by some deep factors, from the lower crust or the upper mantle.

From the measurements at these seven stations, the seismic velocity changes in the different period bands all show Tohoku-oki earthquake-related velocity decreases at different locations. Velocity changes in different period bands show different distance-dependent characteristics. When the interdistance (i.e., between station and epicenter) increases, the amplitude of the velocity changes decays faster at short periods than at long periods. However, at short periods, the response is stronger. We can still observe coseismic velocity decreases at stations FMIH and ASSH in the volcanic region far from the epicenter, where there is no substantial evidence of velocity changes at long periods.

3.1. Spatial Distribution of the Postseismic Velocity Changes

Assuming that the preseismic velocity fluctuates around 0, we first remove the mean seismic velocity changes before the Tohoku-oki earthquake from the first day of 2008 and compute the mean velocity changes over 6 months following the Tohoku-oki earthquake, from April to September 2011. After averaging at every location of the 190 stations for 100 km, we map the spatial distributions of the mean values using linear interpolation with a resolution of 1 arcmin (~2 km). We repeat this procedure for the three period bands.

Figure 4 illustrates that the seismic responses at the different periods have different spatial distributions. In the period band of 1 to 7 s (Figure 4a), the velocity decreases strongly down to ~ −0.08% in the surrounding region of Miyagi, which is not adjacent to the epicenter of the 2011 M_w 9.0 Tohoku-oki earthquake. The amplitude of the maximum drop decreases outward from the coastal center area around Sendai. In contrast to the velocity changes for the period band of 1 to 7 s, the location with the most substantial velocity changes for the period range of 8 to 30 s is shifted northeast to the coastlines of the southern Iwate and northern Miyagi prefectures (Figure 4b). The most significant absolute velocity drop reaches ~0.05%, which is weaker than that at the shorter periods. For the period band of 15 to 50 s (Figure 4c), the absolute velocity drop is reduced to ~0.025%. The coseismic velocity changes for the period band of 15 to 50 s show smaller amplitudes compared with the other periods. The area with strong velocity changes spreads mostly to the north and south of Honshu. The geographic limits of both of the spatial distributions of the seismic velocity

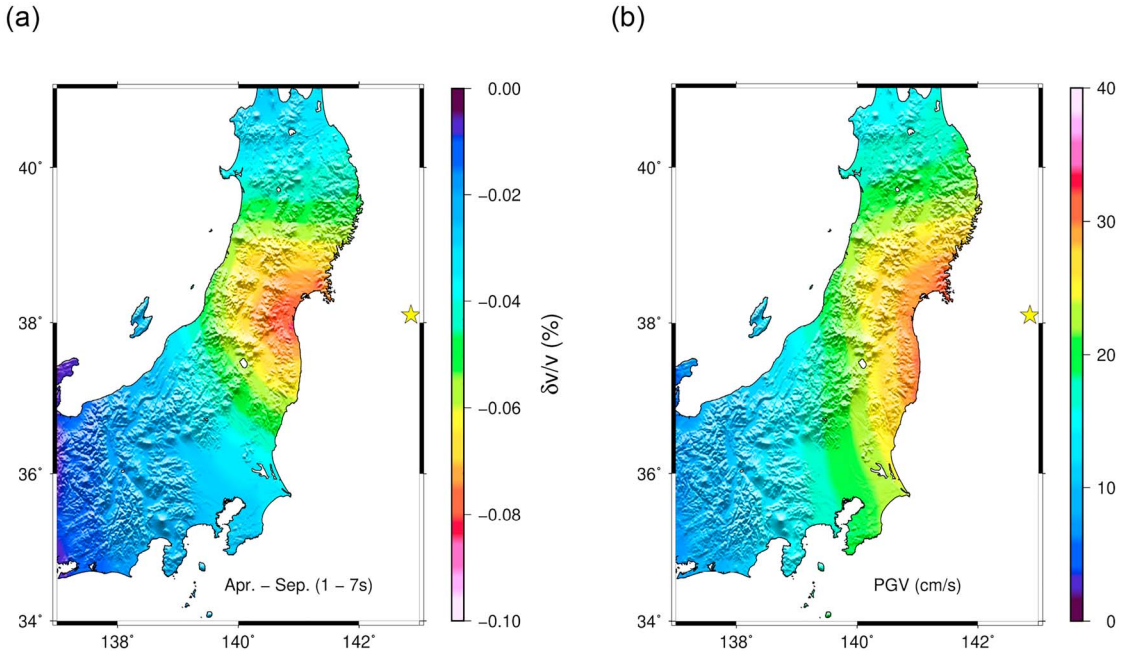

Figure 5. (a) Mean postseismic velocity changes over the months from April to September 2011, in the period range of 1 to 7 s. (b) Map of the peak ground velocity (cm/s) obtained from the square root of the measurements over all three of the components.

changes in the period ranges of 8 to 30 s and 15 to 50 s are at the volcanic front associated with the subduction of the Pacific Plate. The different features of the distribution of the velocity variations in the different period bands might suggest that the origins of the seismic velocity changes are disparate.

To clarify the main origins of the velocity changes in the different period ranges, we compare the maps of the seismic velocity changes with the maps of both the peak ground velocity and the deformation in the crust. Figure 5 shows the velocity changes for the short-period band of 1 to 7 s and the root summed squares of the peak ground velocity measured from three downhole components. Both of these are smoothed over 100 km before the mapping. The spatial distribution of the postseismic velocity changes shows similarities with the regions of the strong shaking. This similarity suggests that the seismic velocity changes at short periods are sensitive to changes in the medium due to shaking and lightly related to the nonlinear behavior of the superficial unconsolidated shallow layers. This suggestion is consistent with the conclusions for the seismic velocity susceptibility by Brenguier et al. (2014), which is the ratio between the changes in the seismic velocity ($\delta v/v$) and the dynamic stress $\Delta\sigma$, as $\frac{\delta v/v}{\Delta\sigma}$, where $\Delta\sigma \sim \dot{u}(t)$ (peak ground velocity). We note here that the crustal seismic velocity decrease is related to the mechanical weakening of the crust by the dynamic stress associated with the seismic waves. Also Sawazaki et al. (2015) concluded that shallow damage is the predominant factor for short-period seismic velocity changes.

Figure 6 shows the map of the modeled seismic velocity changes for the period band of 8 to 30 s, and the map of the coseismic dilatation at 20 km in depth. The coseismic dilatation is calculated using a three-dimensional (3-D) depth-dependent viscoelastic finite element model based on the GPS displacements (Becker et al., 2018; Freed et al., 2017). Both of these maps are smoothed over 100 km before mapping. We observe that the area of maximum velocity drop is shifted to the northeast with respect to the result for the period range of 1 to 7 s and is in agreement with the spatial distribution of the coseismic static strain. The different temporal evolution and different spatial distribution of the seismic velocity changes indicate different behaviors at the different depths probed by these measurements. A first-order conclusion is that there are specific changes at depth that are different from those in the shallow layers, which are likely to be dominated by strong shaking. In the following, we quantitatively investigate the depth dependence of the seismic velocity changes.

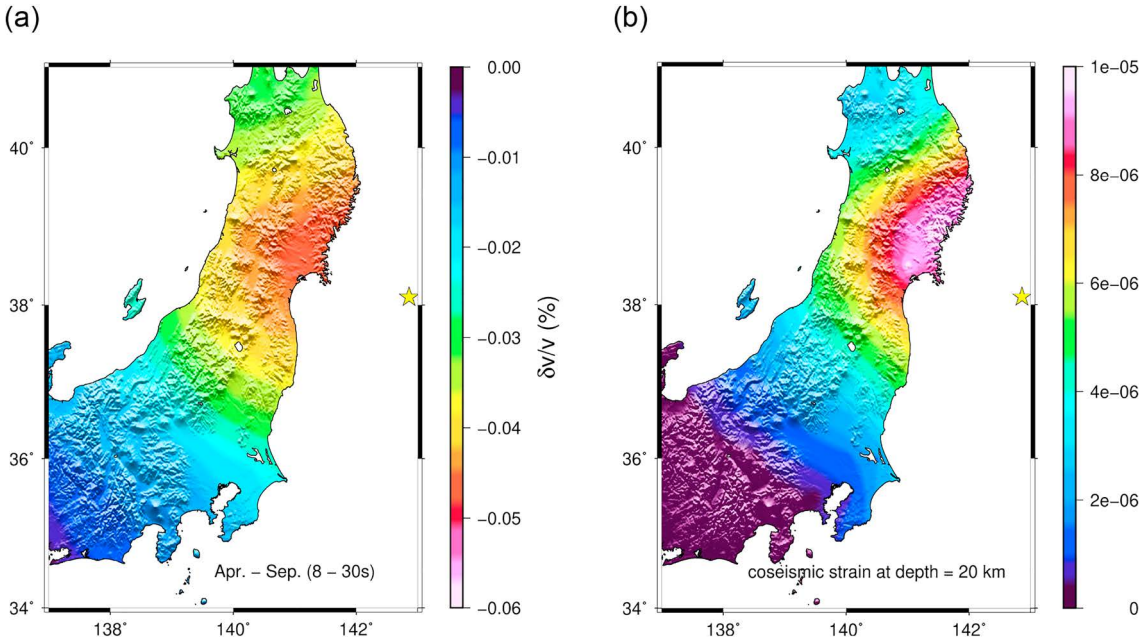

Figure 6. (a) Mean postseismic velocity changes over the months from April to September 2011, for the period range of 8 to 30 s. (b) Modeled coseismic static strain at the depth of 20 km.

3.2. Temporal Variation of Seismic Velocity at Depth

3.2.1. Averaged Seismic Velocity Changes

In all, 74 Hi-net stations in the most affected area (Figure 7a, red trapezoidal shaded zone) were selected to measure the averaged temporal evolution in the four period ranges of 1 to 7 s, 8 to 16 s, 15 to 30 s, and 20 to 50 s. Figure 7b shows the monthly averaged time series of the seismic velocity changes for the four period bands. We take the averaged measurements from all station pairs having at least one station located in the red shaded zone (Figure 7a). To avoid the potential seasonal effects, for 1 to 7 s, we use the results corrected from hydrometeorological forcing by Wang et al. (2017), for the three longer-period bands, we remove the mean annual signals averaged over the years 2009 and 2010 to exclude the year 2008, when Iwate-Miyagi earthquake may affect the velocities. The error bars are standard deviations calculated using the seismic velocity changes in 2009 to 2010. Overall, the seismic velocity decreases as a result of the Tohoku-oki earthquake. Coseismic responses are of the same order of magnitude (10^{-4}) in the four period bands, and they tend to be smaller as the period increases. Errors tend to be bigger when period increases. However, we can observe that in the 15- to 30-s and 20- to 50-s period bands, velocity continues to decrease after the earthquake. This decrease is highlighted by the yellow shaded rectangle in Figure 7b.

In the period band of 1 to 7 s, the coseismic velocity shows the most changes. The velocity decreases instantaneously after the mainshock and recovers relatively fast, within the first few months. In the period range of 10 to 20 s, the coseismic velocity decreases down to ~0.04% and recovers slowly. For the longer period ranges of 15 to 30 s and 20 to 50 s, it is important to highlight the delayed response. The maximum velocity drop is delayed from the time of earthquake occurrence, with a time lag that depends on the period range, which can be as large as 6 months. The shapes of these curves are different, which suggests again that there are different behaviors at different depths. If the changes in physical properties happened only at the surface, the curves at the different frequencies would have different amplitudes, but the same shape. Therefore, these differences in the shapes imply depth-dependent rheology with nonelastic behavior that extends into the lower crust. This provides further evidence, in addition to the different spatial distributions, of the changes in the different period bands.

A similar delayed minimum was also observed by Froment et al. (2013) for the 2008 Wenchuan earthquake (12 May, M_w 8.0). They reported a delay of ~3 months after the main shock in the period band of 12 to 20 s. The velocities tend to decrease gradually during the first 3 months after the mainshock and reach their minima around July. In contrast with our results, the seismic velocity changes in Wenchuan are more

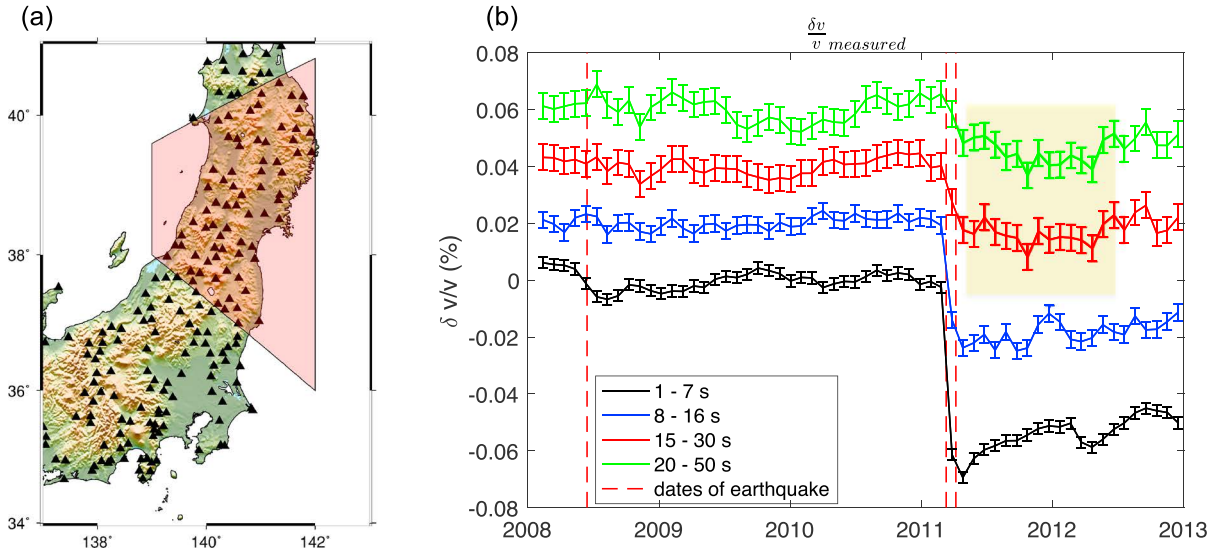

Figure 7. (a) Map of the tiltmeter stations within the red shaded area, where the seismic velocity changes are selected to further study the temporal evolution. (b) Time series of the seismic velocity changes averaged over the stations in the red shaded area for the four period ranges. The time series are shifted by 0.02, 0.04, and 0.06 for period bands 8 to 16 s, 15 to 30 s, and 20 to 50 s, respectively. The yellow shaded rectangle cover the time period of the delayed effects, where velocity continues to decrease.

significant at long periods compared to short periods. This might result from the specific structure, with a low-velocity zone in the Earth crust at depths of 20 to 40 km, as reported by Chen et al. (2018) for this region. The delayed seismic velocity changes in Wenchuan have been argued to be due to the nonlinear viscoelastic seismic responses from the lower crust. Nevertheless, the precise physical meaning of this delay remains unclear.

3.2.2. Inversion of Seismic Velocity Changes Based on Rayleigh Wave Sensitivity Kernels

To better understand these period-dependent seismic velocity changes, we first invert our measurements in the four period bands into a five-layer model that reaches a depth of 40 km. In this study, we measure the seismic velocity changes every 30 days (i.e., monthly) for the four frequency bands, using coda waves. The changes are small enough to be considered as the first-order perturbations. Assuming that surface waves predominate coda waves, the inversion is based on the frequency-dependent Rayleigh wave to *S* wave sensitivity kernels $K_{\mathrm{dc/d}\beta}(f)$, as Rayleigh wave phase velocity of a layered earth model is a function of frequency and *S* wave velocity, *P* wave velocity, and density. However, *S* wave velocities have the dominant influence (Xia et al., 1999) and we invert our results in terms of variations of *S* wave velocity at different depths. We use the velocity model of Matsubara et al. (2017) and take the mean value for calculating $K_{\mathrm{dc/d}\beta}(f)$ in the red shaded area shown in Figure 7a. The detailed inversion process is given in the Appendix.

After inversion, the reconstructed seismic velocity changes (Figure 8b) are very consistent with the measurements. The depth localization of the *S* wave velocity changes $\frac{\delta v_s}{v_s}(t,z)$ is shown in Figures 8a and 8c. We observe that the amplitudes of the changes weaken as the depth increases. At the end of 2012, the velocity changes at different depths have not recovered to their initial states before the earthquake. The delay of the maximum velocity drop appears larger at depth. The substantial velocity changes are mainly located in the shallow layers within 30 km in the crust. Below 30 km, *S* wave changes are not well constrained, because of the loss of resolution due to the shape of the surface wave kernels and because the signal-to-noise ratio of the cross correlations decreases with increasing of the period. From Figure 8a, we can also identify propagation-hood velocity decreases that start from the deepest layer toward the surface, at around the beginning of 2012. We outline this trend with a gray dashed line in Figure 8a.

To verify the impact of random perturbations on the inversion results, we separately add ~10% random noise ($\pm 0.01\%\ \delta v/v$) to the measured data in the different period bands. Then we use the same inversion steps and coefficients to invert the seismic velocity changes from the different period bands into different layers at depth, based on the normalized Rayleigh wave sensitivity kernels, to study the contribution of each period band to the inversion results. Overall, after noise addition, each inversion result can basically reobtain the

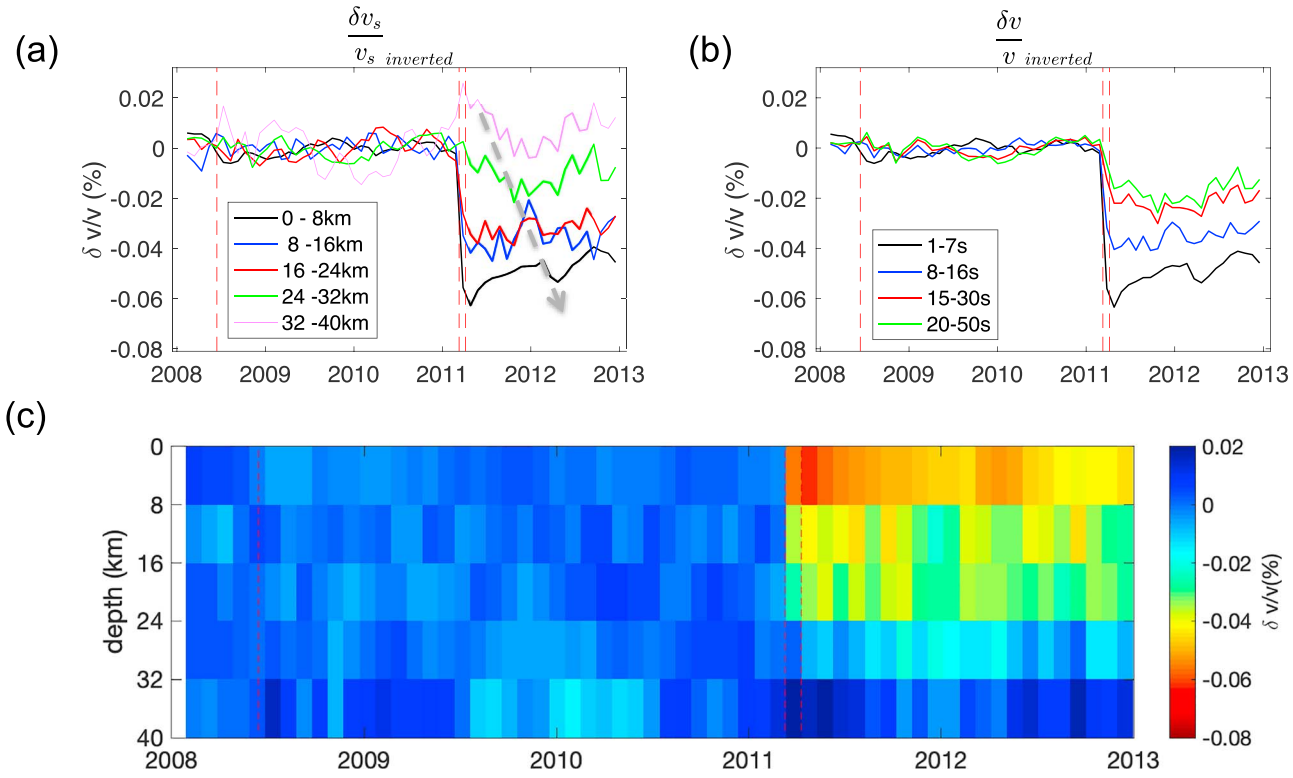

Figure 8. (a) Inverted monthly *S* wave velocity changes versus depth, from 2008 to 2012. The gray dashed line indicates the reduction of seismic velocity from the lower crust to the subsurface. (b) Summation of the inverted seismic velocity changes. (c) Inverted monthly *S* wave velocity changes to 40 km in depth, from 2008 to 2012.

characteristics of the *S* wave velocity variations with depths similar to the previous ones shown in Figure 8c. The detailed perturbation tests are given in section A2.

We have considered so far the sensitivity of Rayleigh waves. In a stratified medium, Love waves have also to be considered when dealing with the surface wave component in the coda, particularly since we use only horizontal components with tiltmeters. Margerin (2009) has studied the mode equipartition in a layered half-space. The author presented in Figure 5 the result for the case of a layer over a half-space that we can consider as a simplified model of crust and mantle for the longer period band considered here. Margerin (2009) showed that Love wave is playing a prominent part for frequencies around the resonance frequency of the upper layer for *S* waves, which is typically corresponding to our longest period band. Although the local structure of the equipartitioned coda field is not giving directly the partition of sensitivity, which depends on the global dynamics of the field (Obermann et al., 2016), it is necessary to evaluate the difference of sensitivity of Rayleigh and Love in our specific case. The inversion results obtained with Love kernels are given in section A2. Although Love wave sensitivity and therefore velocity changes are slightly more concentrated to shallow depth than Rayleigh ones, the global picture of the velocity changes does not change significantly (Figure A5).

3.2.3. Body Wave Sensitivity Kernels

It is important to note that the inversion is under the assumption that the depth sensitivity of the seismic velocity changes is dominated by the surface wave sensitivity. However, we actually measure velocity changes of the coda waves, which are considered to be multiple-scattered waves that are caused by numerous heterogeneities distributed uniformly in the Earth crust. At each time, the coda waves consist of the superposition of complex paths that mix *P* waves, *S* waves, and surface waves.

The sensitivity of coda waves to a velocity change at depth was studied numerically by Obermann et al. (2013) and Obermann et al. (2016), to evaluate the roles of the body and surface waves. They reported that the sensitivity of coda waves ($\mathbf{K}_c$) is from the combination of the sensitivities of both the surface waves ($\mathbf{K}_{sw}$) and the body waves ($\mathbf{K}_{bw}$). $\mathbf{K}_{sw}$ is more important in the early coda, and body waves have an increasing

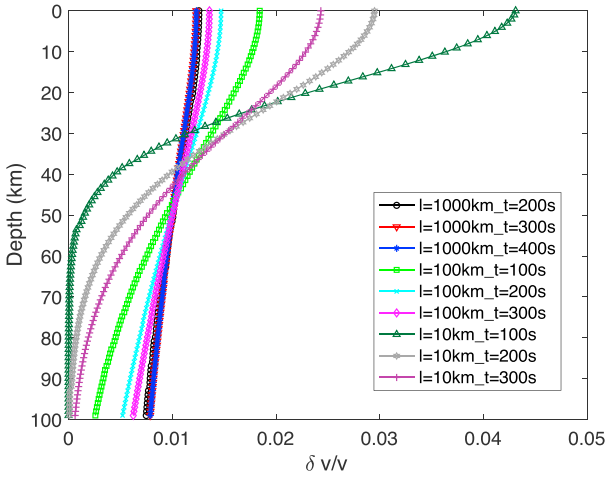

Figure 9. Depth sensitivity of the body waves with different lapse time t and scattering mean free path l for an area with length, width, and depth of 1,000, 1,000, and 100 km, respectively, and for total velocity change = 1.

importance in the later coda. For long periods, the transport mean free time $t^\star$ is large (100 s). As we measure the velocity changes at around a lapse time of 400 s at long periods, we are in the case of the early coda, where the sensitivity is dominated by that of the Rayleigh waves. With this proviso, $\mathbf{K}_c$ is controlled by $\mathbf{K}_{sw}$ in long-period ranges. To be more precise, (Obermann et al., 2013, 2016) showed that the sensitivities obey the following relationship:

$$\mathbf{K}_c = \alpha \mathbf{K}_{sw} + (1-\alpha)\mathbf{K}_{bw}, \quad (1)$$

where α is the partition coefficient. The estimation of the partition coefficients requires numerical simulation. Obermann et al. (2016) indicated the importance of $\mathbf{K}_{sw}$ for the first six mean free times, and the increased importance of $\mathbf{K}_{bw}$ with increasing time. This confirms our choice of using surface wave sensitivities. $\alpha = 1$ in equation (1) is an extreme case. It means our measurement has a very short normalized time, when $\mathbf{K}_c$ depends totally on the surface wave sensitivity kernels $\mathbf{K}_{sw}$.

It would be more precise to consider that for the coda waves that we use, the depth sensitivities depend on the sensitivities of both the surface and body waves. As the precise values for $t^\star$ and α are not available, we evaluate the implication of our hypothesis by considering the case of scattered body waves.

We consider a 3-D sensitivity kernel formulation (Planès et al., 2014) based on the exact solution of the radiative transfer equation for isotropic scattering (Paasschens, 1997), to evaluate the theoretical depth sensitivity of the body wave velocity changes $\delta v/v_{body}$. We state the details and the parameters used regarding the body wave depth sensitivity calculations in the Appendix. Figure 9 gives the normalized depth sensitivities of the body wave velocity changes $\delta v/v_{body}$ with various combinations of scattering mean free path l and lapse time t. We take the mean free path similar to the orders of magnitude estimated by Sato (1978) and by Aki and Chouet (1975) at different frequencies, in Japan.

From the result, we can observe that when the mean free path is taken as unrealistically small, as 10 km for short-period measurements with lapse time t = 100, 200, and 300 s, the body waves are more sensitive to the upper crust. However, the penetrating depth is already deeper than surface wave sensitivity kernels. Furthermore, the sensitivity gets deeper with increasing lapse time in the coda. When using longer and more realistic mean free paths, such as the 100 and 1,000 km considered for long-period measurements, the depth sensitivities of the body waves are more sensitive to the deep part, than when using the 10-km mean free path. All of the sensitivities are similar, and have a nonnegligible important portion at more than 40 km in depth. This is very different from the surface wave sensitivity kernels, where the sensitivity decreases rapidly with depth.

Therefore, for body waves, the depth sensitivities have more weight at greater depth than when considering surface waves. We measure the seismic velocity changes until 400 s for the tiltmeter data at relatively long periods. Thus, the inverted velocity changes would be deeper if we had considered body wave sensitivity rather than Rayleigh wave sensitivity. Our measurements in the period range of 1 to 50 s should reflect the velocity changes at greater depths, if body waves are considered. It can be noted that in our case the assumption of surface wave sensitivity leads to an underestimation of the depth of the temporal changes in the physical properties.

4. Discussion

We want to understand the physical processes that control depth-dependent seismic velocity changes, especially for delayed postseismic responses at depth. For seismic velocity changes at shallow depths, the seismic velocity changes are controlled by the dynamic perturbations from the earthquake. The instantaneous coseismic drop followed by a long-term postseismic relaxation can be explained by the processes referred to in laboratory experiments as fast and slow dynamics. A physical model was proposed by Sens-Schönfelder et al. (2018).

Explanation of the delayed seismic response should be referred to as geodetic observations. The postseismic deformation of the Tohoku-oki earthquake has been widely studied based on both on-land and offshore GPS observations and numerical modeling. Sun et al. (2014) and Watanabe et al. (2014) considered that the postseismic deformation is controlled by viscoelastic relaxation in the asthenosphere. Ozawa et al. (2011) explained the short-term (2 weeks) postseismic deformation by assuming the dominant effect of afterslip, which occurs deeper than the coseismic slip, while Freed et al. (2017), Hu et al. (2016), and Yamagiwa et al. (2015) suggested the combined effects from both viscoelastic relaxation and afterslip. Freed et al. (2017) explained the postseismic displacements, as vertical and horizontal, on land and offshore, using the combined model of afterslip and viscoelasticity with depth-dependent layered viscosity. All the models share common extension of the continental crust due to the big earthquake. The coseismic change of strain is much larger than the later evolution of the strain due to afterslip and the viscoelastic response in the 2-year period that we study here. The extension itself might lead to the weakening of the crust, thus decreasing the seismic velocity. Also, extension enables the rise of fluid under lithostatic pressure at depth. The fluid diffusion process can also conduct the continuing seismic velocity changes after the earthquake. Nakajima and Uchida (2018) commented that there is repeated fluid transfer from megathrusts. The transfer of fluid that arises from the hydrated slab can reduce the seismic velocity from the lower crust to the subsurface. This might be an important factor that is responsible for the delayed response at large depths. As with GPS observations, seismic velocity responses are subject to the combined effects of viscoelastic deformation from the lower crust, and afterslip occurs in the months following the mainshock and enhanced fluid transport. At this stage, we have no indisputable evidence for a simple process explaining the new observations presented here.

5. Conclusion

We show here for the first time that tiltmeter recordings can be used as broadband seismometers to monitor seismic velocity changes at long periods. The results from the different frequency bands provide us with a good opportunity to study the temporal evolution of depth-dependent seismic velocity changes in the whole crust. A comprehensive analysis at a spatiotemporal scale helps us to better unveil the 2011 Tohoku-oki earthquake-related coseismic and postseismic stress recovery processes.

Distributions of strong velocity decreases at short periods are limited to the areas with strong ground shaking induced by the M_w 9.0 Tohoku-oki earthquake, while the long-period velocity changes correlate well with the modeled static strain deduced from GPS observations.

The temporal evolution of the velocity changes in the different period ranges shows very different seismic responses. The amplitudes of the coseismic velocity changes decrease with increasing period. Velocity changes at greater periods are delayed in time with respect to the date of the earthquake. Using the sensitivity kernels of different period bands of the Rayleigh surface wave, we can measure S wave velocity changes down to 40 km in depth. We observe the unambiguous existence of changes in the seismic properties at depth, covering the whole crust. We show that the seismic velocity changes at depth are very different from those in shallow layers. The dynamic perturbations from the earthquake dominate the changes in the shallow layers. At depth, the delayed velocity decrease indicates that the velocity change cannot be explained simply by the coseismic strain change. The precise physical meanings of this delay should be further studied.

Appendix A: Inversion of Seismic Velocity Changes Based on Rayleigh Wave Sensitivity Kernels

The inversion problem is expressed as

$$\underset{M\times 1}{d} = \underset{M\times N}{G}\ \underset{N\times 1}{m}, \tag{A1}$$

where d is the observation vector that consists of $\delta v/v$ in the four different period ranges. $\delta v/v_{f_i,t_M}$ are the velocity changes in frequency band i and in month t, that are small enough to be considered as perturbations of the velocity. The parameter m is the model of the veloci ty changes in each layer at depth. Therefore, for the velocity changes in each month, if we invert the seismic velocity changes into five layers,

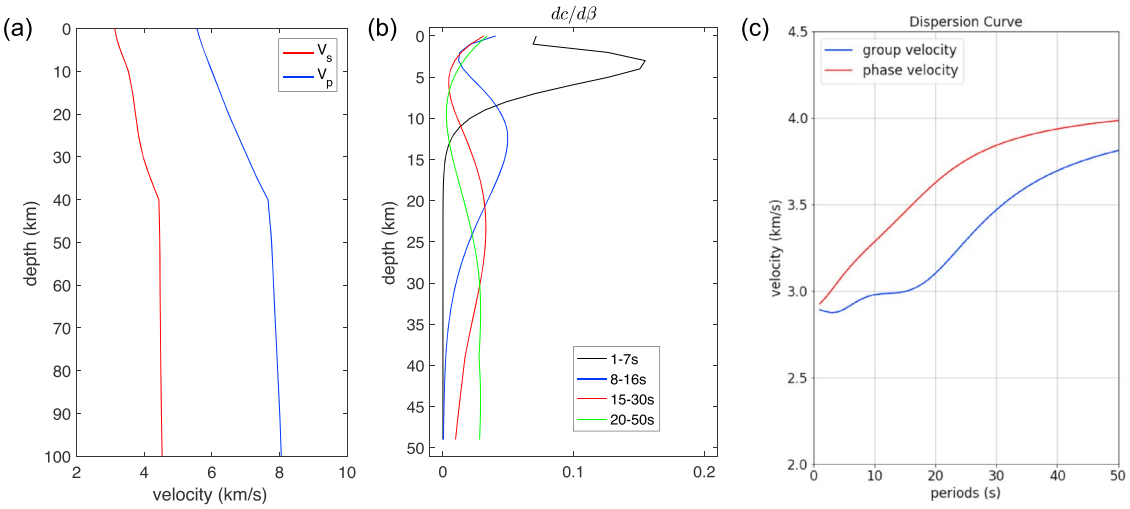

Figure A1. (a) The averaged velocity model after interpolating at 1-km resolution. (b) The normalized sensitivity kernels of the median period in different period ranges. (c) The dispersion curves of the fundamental mode of the Rayleigh waves from the averaged velocity model.

the relationship (A1) turns into a linear system:

$$\begin{bmatrix} \delta v/v_{f_1,t} \\ \delta v/v_{f_2,t} \\ \delta v/v_{f_3,t} \\ \delta v/v_{f_4,t} \end{bmatrix} = \begin{bmatrix} K'_{f_1,d_1} & K'_{f_1,d_2} & K'_{f_1,d_3} & K'_{f_1,d_4} & K'_{f_1,d_5} \\ K'_{f_2,d_1} & K'_{f_2,d_2} & K'_{f_2,d_3} & K'_{f_2,d_4} & K'_{f_2,d_5} \\ K'_{f_3,d_1} & K'_{f_3,d_2} & K'_{f_3,d_3} & K'_{f_3,d_4} & K'_{f_3,d_5} \\ K'_{f_4,d_1} & K'_{f_4,d_2} & K'_{f_4,d_3} & K'_{f_4,d_4} & K'_{f_4,d_5} \end{bmatrix} \begin{bmatrix} \delta v_s/v_{sd_1,t} \\ \delta v_s/v_{sd_2,t} \\ \delta v_s/v_{sd_3,t} \\ \delta v_s/v_{sd_4,t} \\ \delta v_s/v_{sd_5,t} \end{bmatrix}, \tag{A2}$$

where $K'_{f_i,d_j} = K_{f_i,d_j} \times \frac{\beta_{d_j}}{c_{f_i}}$ and is deduced from

$$\begin{aligned} dc_{f_i} &= K_{f_i,d_j} \times d\beta_{d_j} \\ \frac{dc}{c}_{f_i} &= K_{f_i,d_j} \times \frac{\beta_{d_j}}{c_{f_i}} \times \frac{d\beta}{\beta}_{d_j} \\ \frac{dc}{c}_{f_i} &= K'_{f_i,d_j} \times \frac{d\beta}{\beta}_{d_j} \\ \Rightarrow K'_{f_i,d_j} &= K_{f_i,d_j} \times \frac{\beta_{d_j}}{c_{f_i}}. \end{aligned} \tag{A3}$$

β_{d_j} and c_{f_i} are defined as the mean values within the jth layer and in the ith period band, respectively. K_{f_i,d_j} indicates the surface wave sensitivity kernels in frequency band i (Figure A1b) and at a certain depth j for each layer. We compute the dispersion curves of the fundamental mode of Rayleigh waves (Figure A1c) from the averaged velocity model (Figure A1a).

Equation (A2) is an underdetermined system without prior information. To solve the problem, we adopt the damped least squares method. The resolution operator R, which is referred to as the model resolution matrix or the resolving kernel, describes the relationship between the true m_{true} and m from the inversion, where $m = Rm_{\text{true}}$. The perfect R should be equal to I, the identity matrix. R takes the form of

$$R = G^{-g}G, \tag{A4}$$

where G^{-g} is $\left(G^TG + \epsilon^2 I\right)^{-1}G^T$, as the generalized inverse. The damping coefficient for this inversion is fixed as $\epsilon = 0.13$ according to Figure A2, through a search for the inflection point. Velocity changes in different months are independent and share the same sensitivity kernels K. Thus, R is a 5×5 matrix, and the same for seismic velocity changes at different times. The resolution kernel in each layer for each time t is shown in Figure A3. The diagonal values of R are the largest for each layer. According to Figure A3, the first three

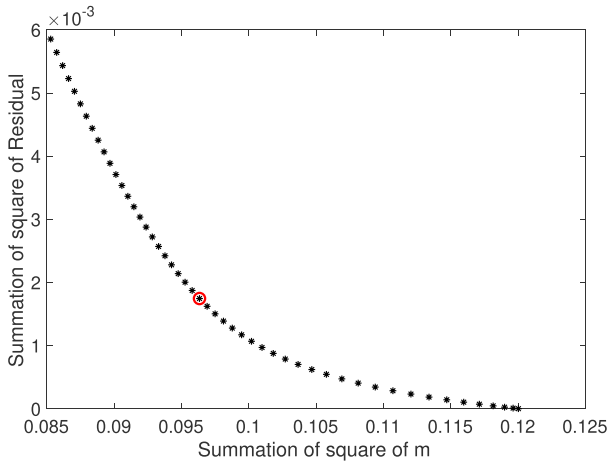

Figure A2. Summed residual versus summed m for searching the best-fit normal damping coefficient ϵ. The red circle indicates $\epsilon = 0.13$, which is used for the inversion.

layers can be better inverted than the last two deep layers. The first layer has the best resolution. The process is repeated for each time step of 1 month, from 2008 to 2012.

A1. Inversion With Perturbations

Figures A4a, A4c, A4e, and A4g show the measured seismic velocity changes in the four period ranges after adding 0.01% random noise (~10% $\delta v/v$) in the different period bands of 1 to 7 s, 8 to 16 s, 15 to 30 s, and 20 to 50 s, respectively. Figures A4b, A4d, A4f, and A4h give the results of the inverted S wave velocity changes from the surface down to 40 km in depth.

In contrast, we can summarize how the 0.01% random perturbations affect the inversion results. Separately, the short-period (1–7 s) interference only has a large impact on the inversion results of the first layer, as the deep results hardly change. The changes in the other period ranges show the same features as for the period range of 1 to 7 s. Perturbations in the period range of 8 to 16 s have a large impact on the second layer, while those of 15 to 30 s have a large impact on the third layer, and those of 20 to 50 s have an impact on both the fourth and fifth layers. The addition of noise in the period range of 15 to 30 s generates the largest interference with the inversion results.

A2. Inversion Based on the Love Wave Sensitivity Kernels

The inversion result based on the Love wave sensitivity kernels shows similar characteristics to the S wave velocity changes versus depth. The coseismic velocity changes decrease with increasing depth. Delay of the maximum velocity drop increases with depth. However, seismic velocity changes for the relatively

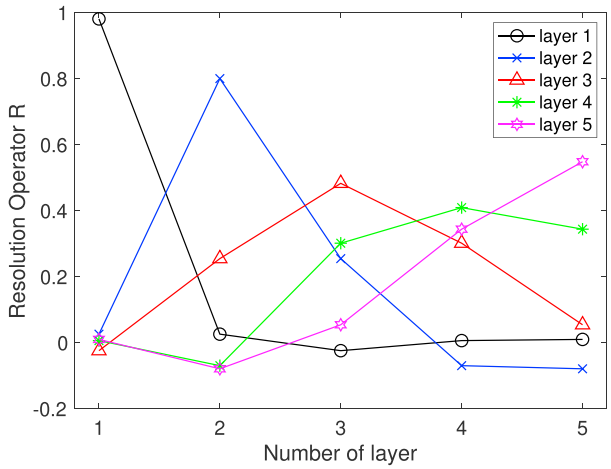

Figure A3. The resolution operators R for the $\delta v_s/v_s$ within five layers.

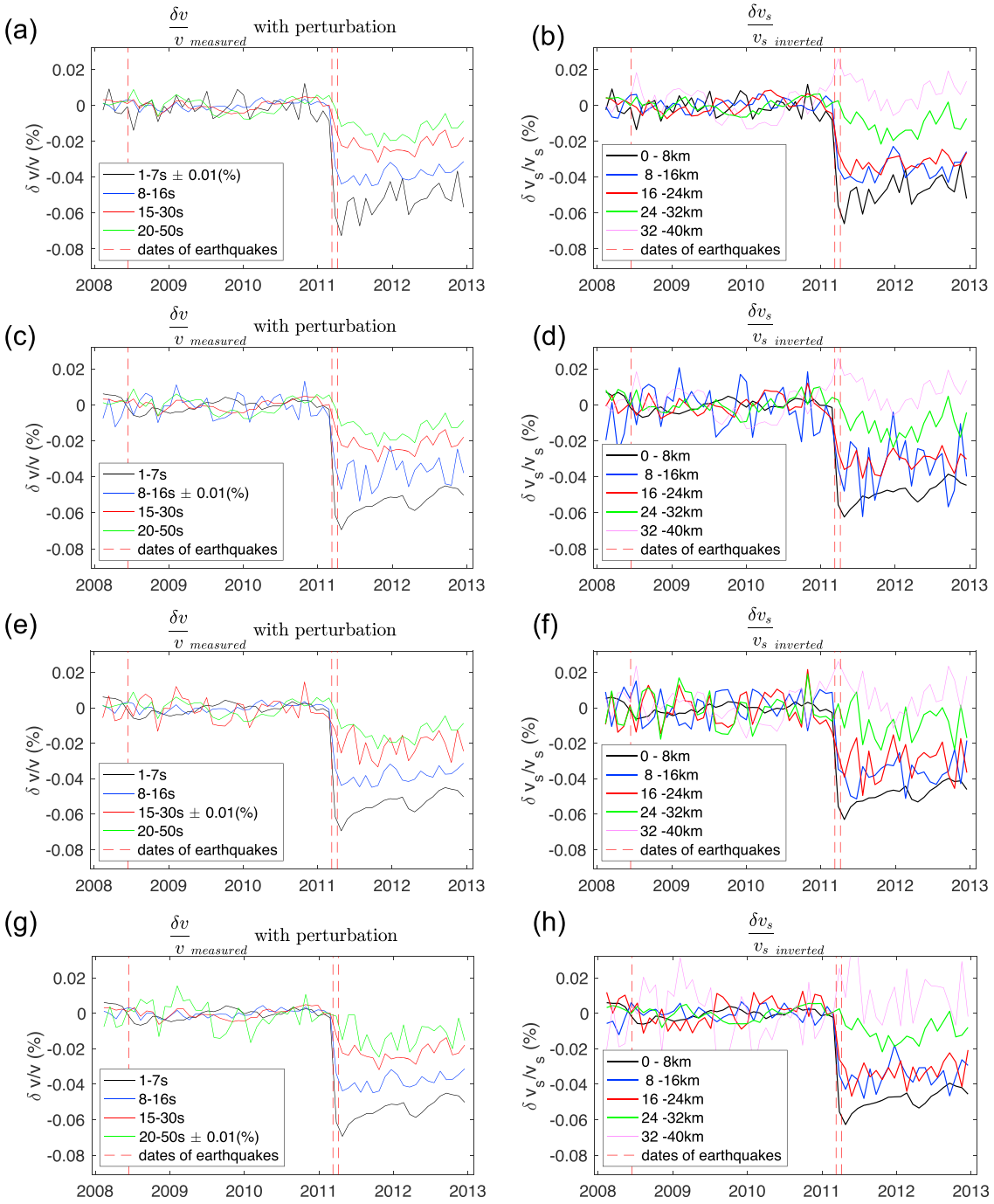

Figure A4. (a) Measured monthly seismic velocity changes in the four period ranges. (b) Measured monthly seismic velocity changes in the four period ranges after adding 0.01% random perturbation in the 1- to 7-s period range. (c) Inverted monthly *S* wave velocity changes versus depth from 2008 to 2012. (d) Summation of the inverted seismic velocity changes. (e) Inverted monthly *S* wave velocity changes from 2008 to 2012, down to 40 km in depth.

long-period ranges (15–30 s, 20–50 s) are not well recovered (Figure A5c) after inversion, as Love waves are more sensitive and concentrated in the shallow depths of the crust. The located *S* wave velocity changes appear relatively shallow compared to those using Rayleigh wave sensitivity kernels, which usually have a maximum sampling depth of about one third of their wavelength.

A3. Body Wave Sensitivity Kernels

To accurately evaluate the sensitivity of the coda body waves, we need to calculate $\mathbf{K}_{bw}$ in terms of the probability of intensity *P*. We follow the 3-D $\mathbf{K}_{bw}$ sensitivity method of Obermann et al. (2013), Planès et al. (2014),

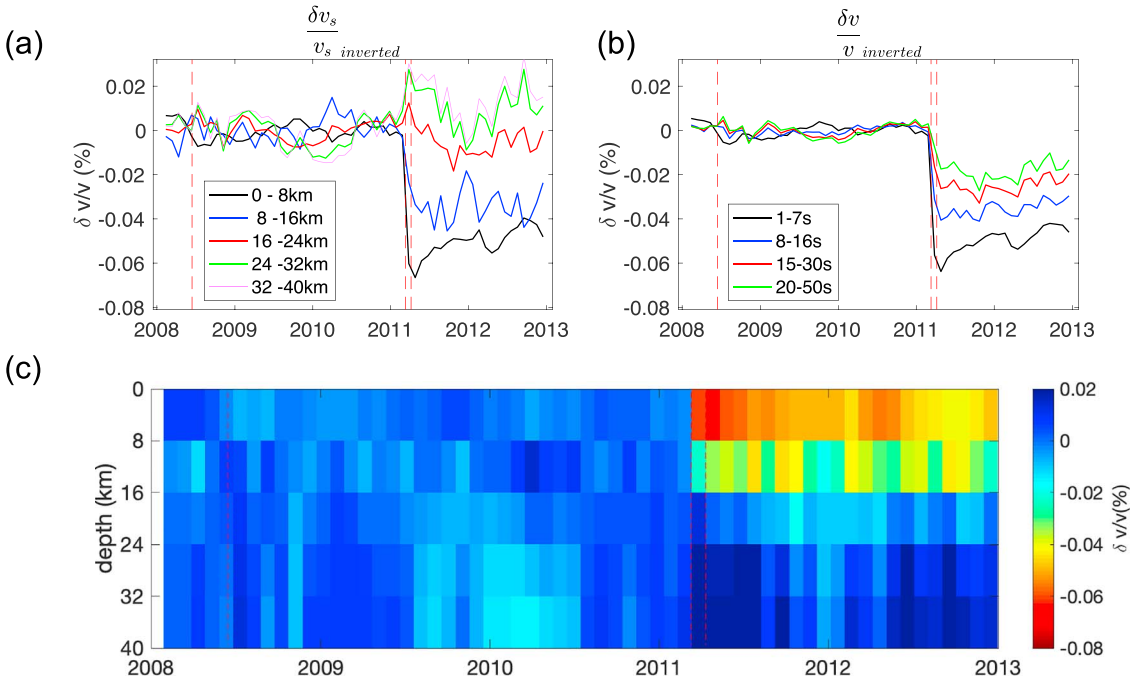

Figure A5. (a) Inverted monthly *S* wave velocity changes versus depth, from 2008 to 2012. (b) Summation of the inverted seismic velocity changes. (c) Inverted monthly *S* wave velocity changes, from 2008 to 2012, down to 40 km in depth.

and Obermann et al. (2016) and start with the definition of the kernel $\mathbf{K}_{\mathrm{bw}}$ of Pacheco and Snieder (2005) (equation (A5)) to calculate the 3-D body sensitivity.

$$\mathbf{K}_{\mathrm{bw}}\left(\mathbf{r}', \mathbf{r}, \mathbf{s}, t\right) = \frac{1}{P\left(\mathbf{r}, \mathbf{s}, t\right)} \int_0^t P\left(\mathbf{r}, \mathbf{r}', t - t'\right) P\left(\mathbf{r}', \mathbf{s}, t'\right) \mathrm{d}t', \tag{A5}$$

where P describes the probability of the intensity of a pulse of energy that propagates through the medium at the distance $\mathbf{r}'$ ($\mathbf{r}' = \mathbf{r}$ at the receiver) and at time t. The approximate solution of the intensity propagator to a diffusion equation solution in three dimensions can be expressed as equation (A6).

$$P\left(\mathbf{s}, \mathbf{r}, t\right) = \frac{1}{(4\pi D t)^{d/2}} \exp\left(\frac{-|\mathbf{r} - \mathbf{s}|^2}{4Dt}\right), \tag{A6}$$

where D represents the diffusion constant and is equal to $\frac{cl^\star}{d}$. The parameter d is the dimension, which is equal to 3 when in three dimensions. This is an analytical solution that can be used to calculate the Kernel sensitivity. The intensity propagator can also be represented as the solution of the radiative transfer equation (Paasschens, 1997), and as an interpolation of the 2-D and 4-D analytic solutions (Planès et al., 2014). Unlike the diffusion propagator, which is valid only when time t is much larger than the transport mean free time $t^\star$, which is equal to $l^\star/c$, where $l^\star$ is the transport mean free path, the radiative transfer solution has a general validity at all lapse times (Planès et al., 2014; Obermann et al., 2016).

The energy velocity c is determined by the equipartition state. As the lapse time increases, the total energy of the P wave and S wave modes reach stable so-called equipartition states. The energy ratio between the S waves and P waves is $\frac{E_s}{E_p}$ and is represented by x. The total energy can be expressed as

$$\begin{aligned} E &= E_p + E_s = E_p + xE_p \\ E &= \frac{E}{1+x} + \frac{x}{1+x}E. \end{aligned} \tag{A7}$$

For elastic wave scattering, the energy ratio x is $2\gamma_0^3$, where γ_0 is the velocity ratio and $\equiv \alpha_0/\beta_0$. The velocity c is finally determined by a weighted average, according to equation (A8), by taking the theoretical equipartition ratio as 10.4, when $\gamma_0 = \sqrt{3}$ for a Poisson solid (Margerin et al., 2000; Weaver, 1982) for further

calculation.

$$\frac{1}{c} = \frac{1}{\beta_0}\frac{1}{(1+x)} + \frac{1}{\alpha_0}\frac{x}{(1+x)}. \tag{A8}$$

The total traveltime in three dimensions over volume V can be expressed as (Pacheco & Snieder, 2005)

$$t = \int_V \mathbf{K}_{\mathrm{bw}}\left(\mathbf{r}', \mathbf{r}, \mathbf{s}, t\right) \mathrm{d}V\left(\mathbf{r}'\right). \tag{A9}$$

The perturbation of the traveltime δt can be expressed as

$$\delta t = \int_V \mathbf{K}_{\mathrm{bw}}\left(\mathbf{r}', \mathbf{r}, \mathbf{s}, t\right) \frac{\delta s_l}{s_l}\left(\mathbf{r}'\right) \mathrm{d}V\left(\mathbf{r}'\right), \tag{A10}$$

where s_l is the slowness. We can replace the left side of equation (A10) by $\delta t = -\frac{\delta v}{v}_{\mathrm{bw}} t$. As the slowness perturbation $\frac{\delta s_l}{s_l}(\mathbf{r}') = -\frac{\delta v}{v}(\mathbf{r}')$, so this can be written as

$$-\frac{\delta v}{v}_{\mathrm{bw}} t = -\int_V \mathbf{K}_{bw}\left(\mathbf{r}', \mathbf{r}, \mathbf{s}, t\right) \frac{\delta v}{v}\left(\mathbf{r}'\right) \mathrm{d}V\left(\mathbf{r}'\right). \tag{A11}$$

In the case of homogeneous velocity changes $\frac{\delta v}{v}$ in each layer of volume V_i from the surface to depth, the measured body wave velocity changes $\frac{\delta v}{v}_{\mathrm{bw}}$ can be expressed as the sum of the integral of the velocity perturbation over all (i) elementary volumes $\mathrm{d}V(z_i)$ at depth. We assume that in each layer of volume V_i, the velocity perturbation $\frac{\delta v}{v}(z_i)$ is constant. In each layer, there is an integral over $\mathrm{d}V_i$

$$\frac{\delta v}{v}_{bw} = \sum_i \int_{V_i} \frac{\mathbf{K}_{bw}(z_i)}{t} \frac{\delta v}{v}(z_i) \mathrm{d}V_i. \tag{A12}$$

Thus, the body wave velocity change is the summation of the perturbation $\frac{\delta v}{v}(z_i)$ multiplied by the weight that is given by the sensitivity kernel in each layer, over the total traveltime.

To calculate the body wave depth sensitivity in this study, we take the energy velocity c (mixed P waves and S waves) as 3.89 km/s, according to formula (A6), and the interdistance of source and receiver as 50 km. Assuming the velocity perturbation $\frac{\delta v}{v}(z_i)$ is 1 in a 1-km layer ($\mathrm{d}V(z_i)$), down to 100 km at depth, we compute the sensitivity $\mathbf{K}$ by testing the different scattering mean free paths l (km) and lapse time t (s) in the coda diffusion.

Acknowledgments
The authors would like to thank Aoki Yosuke for contributions to the peak ground velocity measurements and Anne Obermann for discussion and support on the body waves sensitivity calculation. We also would like to thank Thorsten W. Becker and Andrew M. Freed for their contributions to the numerical geodetic model. Data availability: Hi-net seismic data required in the paper are available from the National Research Institute for Earth Science and Disaster Prevention (NIED, http://www.hinet.bosai.go.jp). Most of the computations presented in this paper were performed using the GRICAD infrastructure (https://gricad.univ-grenoble-alpes.fr), which is partly supported by the Equip@Meso project (reference ANR-10-EQPX-29-01) of the program Investissements d'Avenir supervised by the Agence Nationale pour la Recherche. This project received funding from the European Research Council (ERC) under the European Union Horizon 2020 Research and Innovation Program (Grant Agreement 742335, F-IMAGE; Grant Agreement 817803, FaultScan).

References

Aki, K., & Chouet, B. (1975). Origin of coda waves: Source, attenuation and scattering effects. *Journal of Geophysical Research*, *80*, 3322–3342. https://doi.org/10.1029/JB080i023p03322

Bürgmann, R., & Dresen, G. (2008). Rheology of the lower crust and upper mantle: Evidence from rock mechanics, geodesy, and field observations. *Annual Review of Earth and Planetary Sciences*, *36*(1), 531–567. https://doi.org/10.1146/annurev.earth.36.031207.124326

Becker, T. W., Hashima, A., Freed, A. M., & Sato, H. (2018). Stress change before and after the 2011 *M*9 Tohoku-oki earthquake. *Earth and Planetary Science Letters*, *504*, 174–184. https://doi.org/10.1016/j.epsl.2018.09.035

Brenguier, F., Campillo, M., Hadziioannou, C., Shapiro, N. M., Nadeau, R. M., & Larose, E. (2008). Postseismic relaxation along the San Andreas fault at Parkfield from continuous seismological observations. *Science*, *321*(5895), 1478–1481.

Brenguier, F., Campillo, M., Takeda, T., Aoki, Y., Shapiro, N. M., Briand, X., et al. (2014). Mapping pressurized volcanic fluids from induced crustal seismic velocity drops. *Science*, *345*(6192), 80–82.

Brenguier, F., Shapiro, N. M., Campillo, M., Ferrazzini, V., Duputel, Z., Coutant, O., & Nercessian, A. (2008). Towards forecasting volcanic eruptions using seismic noise. *Nature Geoscience*, *1*(2), 126–130. https://doi.org/10.1038/ngeo104

Campillo, M., & Paul, A. (2003). Long-range correlations in the diffuse seismic coda. *Science*, *299*(5606), 547–549. https://doi.org/10.1126/science.1078551

Chen, J. H., Froment, B., Liu, Q. Y., & Campillo, M. (2010). Distribution of seismic wave speed changes associated with the 12 May 2008 M_w 7.9 Wenchuan earthquake. *Geophysical Research Letters*, *37*, L18302. https://doi.org/10.1029/2010GL044582

Chen, Y., Hu, J., & Peng, F. (2018). Seismological challenges in earthquake hazard reductions: Reflections on the 2008 Wenchuan earthquake. *Science Bulletin*, *63*, 1159–1166. https://doi.org/10.1016/j.scib.2018.06.015

Freed, A. M., Ali, S. T., & Bürgmann, R. (2007). Evolution of stress in Southern California for the past 200 years from coseismic, postseismic and interseismic stress changes. *Geophysical Journal International*, *169*(3), 1164–1179. https://doi.org/10.1111/j.1365-246X.2007.03391.x

Freed, A. M., Bürgmann, R., Calais, E., Freymueller, J., & Hreinsdóttir, S. (2006). Implications of deformation following the 2002 Denali, Alaska, earthquake for postseismic relaxation processes and lithospheric rheology. *Journal of Geophysical Research*, *111*, B01401. https://doi.org/10.1029/2005JB003894

Freed, A. M., Hashima, A., Becker, T. W., Okaya, D. A., Sato, H., & Hatanaka, Y. (2017). Resolving depth-dependent subduction zone viscosity and afterslip from postseismic displacements following the 2011 Tohoku-oki, Japan earthquake. *Earth and Planetary Science Letters*, *459*, 279–290. https://doi.org/10.1016/j.epsl.2016.11.040

Froment, B., Campillo, M., Chen, J. H., & Liu, Q. Y. (2013). Deformation at depth associated with the 12 May 2008 M_w 7.9 Wenchuan earthquake from seismic ambient noise monitoring. *Geophysical Research Letters*, *40*, 78–82. https://doi.org/10.1029/2012GL053995

Fukushima, Y., Toda, S., Miura, S., Ishimura, D., Fukuda, J., Demachi, T., & Tachibana, K. (2018). Extremely early recurrence of intraplate fault rupture following the Tohoku-Oki earthquake. *Nature Geoscience*, *11*, 777–781. https://doi.org/10.1038/s41561-018-0201-x

Gassenmeier, M., Sens-Schönfelder, C., Eulenfeld, T., Bartsch, M., Victor, P., Tilmann, F., & Korn, M. (2016). Field observations of seismic velocity changes caused by shaking-induced damage and healing due to mesoscopic nonlinearity. *Geophysical Journal International*, *204*(3), 1490–1502. https://doi.org/10.1093/gji/ggv529

Hillers, G., Ben-Zion, Y., Campillo, M., & Zigone, D. (2015). Seasonal variations of seismic velocities in the San Jacinto fault area observed with ambient seismic noise. *Geophysical Journal International*, *202*, 920–932. https://doi.org/10.1093/gji/ggv151

Hillers, G., Campillo, M., & Ma, KF (2014). Seismic velocity variations at TCDP are controlled by MJO driven precipitation pattern and high fluid discharge properties. *Earth and Planetary Science Letters*, *391*, 121–127. https://doi.org/10.1016/j.epsl.2014.01.040

Hillers, G., Retailleau, L., Campillo, M., Inbal, A., Ampuero, J. P., & Nishimura, T. (2015). In situ observations of velocity changes in response to tidal deformation from analysis of the high-frequency ambient wavefield. *Journal of Geophysical Research: Solid Earth*, *120*, 210–225. https://doi.org/10.1002/2014JB011318

Hu, Y., Bürgmann, R., Uchida, N., Banerjee, P., & Freymueller, J. T. (2016). Stress-driven relaxation of heterogeneous upper mantle and time-dependent afterslip following the 2011 Tohoku earthquake. *Journal of Geophysical Research B: Solid Earth*, *121*, 385–411. https://doi.org/10.1002/2015JB012508

Mao, S., Campillo, M., van der Hilst, R. D., Brenguier, F., Stehly, L., & Hillers, G. (2019). High temporal resolution monitoring of small variations in crustal strain by dense seismic arrays. *Geophysical Research Letters*, *46*, 128–137. https://doi.org/10.1029/2018GL079944

Margerin, L. (2009). Generalized eigenfunctions of layered elastic media and application to diffuse fields. *The Journal of the Acoustical Society of America*, *125*, 164–174. https://doi.org/10.1121/1.3021312

Margerin, L., Campillo, M., & Van Tiggelen, Bart (2000). Monte Carlo simulation of multiple scattering of elastic waves. *Journal of Geophysical Research*, *105*, 7873–7892. https://doi.org/10.1029/1999JB900359

Matsubara, M., Sato, H., Uehira, K., Mochizuki, M., & Kanazawa, T. (2017). Three-dimensional seismic velocity structure beneath Japanese islands and surroundings based on NIED seismic networks using both inland and offshore events. *Journal of Disaster Research*, *12*, 844–857. https://doi.org/10.20965/jdr.2017.p0844

Meier, U., Shapiro, NM, & Brenguier, F. (2010). Detecting seasonal variations in seismic velocities within Los Angeles basin from correlations of ambient seismic noise. *Geophysical Journal International*, *181*(2), 985–996. https://doi.org/10.1111/j.1365-246X.2010.04550.x

Minato, S., Tsuji, T., Ohmi, S., & Matsuoka, T. (2012). Monitoring seismic velocity change caused by the 2011 Tohoku-oki earthquake using ambient noise records. *Geophysical Research Letters*, *39*, L09309. https://doi.org/10.1029/2012GL051405

Nakajima, J., & Uchida, N. (2018). Repeated drainage from megathrusts during episodic slow slip. *Nature Geoscience*, *11*, 351–356. https://doi.org/10.1038/s41561-018-0090-z

Nishida, K., Kawakatsu, H., & Obara, K. (2008). Three-dimensional crustal Swave velocity structure in Japan using microseismic data recorded by Hi-net tiltmeters. *Journal of Geophysical Research*, *113*, B10302. https://doi.org/10.1029/2007JB005395

Obara, K., Kasahara, K., Hori, S., & Okada, Y. (2005). A densely distributed high-sensitivity seismograph network in Japan:Hi-net by National Research Institute for Earth Science and Disaster Prevention. *Review of Scientific Instruments*, *76*(2), 021301. https://doi.org/10.1063/1.1854197

Obermann, A., Froment, B., Campillo, M., Larose, E., Planès, T., Valette, B., et al. (2014). Seismic noise correlations to image structural and mechanical changes associated with the M_w 7.9 2008 Wenchuan earthquake. *Journal of Geophysical Research: Solid Earth*, *119*, 3155–3168. https://doi.org/10.1002/2013JB010932

Obermann, A., Planès, T, Hadziioannou, C., & Campillo, M. (2016). Lapse-time-dependent coda-wave depth sensitivity to local velocity perturbations in 3-D heterogeneous elastic media. *Geophysical Journal International*, *207*(1), 59–66. https://doi.org/10.1093/gji/ggw264

Obermann, A., Planès, T., Larose, E., Sens-Schönfelder, C., & Campillo, M. (2013). Depth sensitivity of seismic coda waves to velocity perturbations in an elastic heterogeneous medium. *Geophysical Journal International*, *194*(1), 372–382. https://doi.org/10.1093/gji/ggt043

Obermann, A., Planés, T., Larose, E., & Campillo, M. (2018). 4-D imaging of subsurface changes with coda waves: Numerical studies of 3-D combined sensitivity kernels and applications to the M_w 7.9, 2008 Wenchuan earthquake. *Pure and Applied Geophysics*, *176*, 1243–1254. https://doi.org/10.1007/s00024-018-2014-7

Okada, Y., Kasahara, K., Hori, S., Obara, K., Sekiguchi, S., Fujiwara, H., & Yamamoto, A. (2004). Recent progress of seismic observation networks in Japan—Hi-net, F-net, K-net and KiK-net -. *Earth, Planets and Space*, *56*(8), xv–xxviii. https://doi.org/10.1186/BF03353076

Ozawa, S., Nishimura, T., Suito, H., Kobayashi, T., Tobita, M., & Imakiire, T. (2011). Coseismic and postseismic slip of the 2011 magnitude-9 Tohoku-Okiearthquake. *Nature*, *475*(7356), 373–377. https://doi.org/10.1038/nature10227

Paasschens, J. (1997). Solution of the time-dependent Boltzmann equation. *Physical Review E*, *56*, 1135–1141. https://doi.org/10.1103/PhysRevE.56.1135

Pacheco, C., & Snieder, R. (2005). Time-lapse travel time change of multiply scattered acoustic waves. *The Journal of the Acoustical Society of America*, *118*, 1300–1310. https://doi.org/10.1121/1.2000827

Planès, T., Larose, E., Margerin, L., Rossetto, V., & Sens-Schönfelder, C. (2014). Decorrelation and phase-shift of coda waves induced by local changes: Multiple scattering approach and numerical validation. *Waves in Random and Complex Media*, *24*, 99–125. https://doi.org/10.1080/17455030.2014.880821

Pollitz, F. F. (1992). Postseismic relaxation theory on the spherical earth. *Bulletin of the Seismological Society of America*, *82*(1), 422–453.

Pollitz, F. F. (2005). Transient rheology of the upper mantle beneath central Alaska inferred from the crustal velocity field following the 2002 Denali earthquake. *Journal of Geophysical Research*, *110*, B08407. https://doi.org/10.1029/2005JB003672

Rivet, D., Campillo, M., Radiguet, M., Zigone, D., Cruz-Atienza, V., Shapiro, N. M., et al. (2013). Seismic velocity changes, strain rate and non-volcanic tremors during the 2009-2010 slow slip event in Guerrero, Mexico. *Geophysical Journal International*, *196*(1), 447–460. https://doi.org/10.1093/gji/ggt374

Sato, H. (1978). Mean free path of *S*-waves under the Kanto district of Japan. *Journal of Physics of the Earth*, *26*, 185–198. https://doi.org/10.4294/jpe1952.26.185

Sawazaki, K., Kimura, H., Shiomi, K., Uchida, N., Takagi, R., & Snieder, R. (2015). Depth-dependence of seismic velocity change associated with the 2011 Tohoku earthquake, Japan, revealed from repeating earthquake analysis and finite difference wave propagation simulation. *Geophysical Journal International*, *201*(2), 741–763. https://doi.org/10.1093/gji/ggv014

Sens-Schönfelder, C., & Wegler, U. (2006). Passive image interferometry and seasonal variations of seismic velocities at Merapi Volcano, Indonesia. *Geophysical Research Letters*, *33*, L21302. https://doi.org/10.1029/2006GL027797

Sens-Schönfelder, C., Snieder, R., & Li, X. (2018). A model for nonlinear elasticity in rocks based on friction of internal interfaces and contact aging. *Geophysical Journal International*, *216*, 319–331. https://doi.org/10.1093/gji/ggy414

Shapiro, N. M., & Campillo, M. (2004). Emergence of broadband Rayleigh waves from correlations of the ambient seismic noise. *Geophysical Research Letters*, *31*, L07614. https://doi.org/10.1029/2004GL019491

Sun, T., Wang, K., Iinuma, T., Hino, R., He, J., Fujimoto, H., et al. (2014). Prevalence of viscoelastic relaxation after the 2011 Tohoku-oki earthquake. *Nature*, *514*(7520), 84–87. https://doi.org/10.1038/nature13778

Taira, T., & Brenguier, F. (2016). Response of hydrothermal system to stress transients at Lassen Volcanic Center, California, inferred from seismic interferometry with ambient noise. *Earth, Planets and Space*, *68*(1), 162.

Taira, T., Brenguier, F., & Kong, Q. (2015). Ambient noise-based monitoring of seismic velocity changes associated with the 2014 M_w 6.0 South Napa earthquake. *Geophysical Research Letters*, *42*, 6997–7004. https://doi.org/10.1002/2015GL065308

Tonegawa, T., Hirahara, K., & Shiomi, K. (2006). Upper mantle imaging beneath the Japan Islands by Hi-net tiltmeter recordings. *Eath Planet Space*, *58*, 1007–1012. https://doi.org/10.1186/BF03352605

Wang, Q. Y., Brenguier, F., Campillo, M., Lecointre, A., Takeda, T., & Aoki, Y. (2017). Seasonal crustal seismic velocity changes throughout Japan. *Journal of Geophysical Research: Solid Earth*, *122*, 7987–8002. https://doi.org/10.1002/2017JB014307

Watanabe, S. I., Sato, M., Fujita, M., Ishikawa, T., Yokota, Y., Ujihara, N., & Asada, A. (2014). Evidence of viscoelastic deformation following the 2011 Tohoku-Oki earthquake revealed from seafloor geodetic observation. *Geophysical Research Letters*, *41*, 5789–5796. https://doi.org/10.1002/2014GL061134

Weaver, R. L. (1982). On diffuse waves in solid media. *The Journal of the Acoustical Society of America*, *71*, 1608–1609. https://doi.org/10.1121/1.387816

Wegler, U., Nakahara, H., Sens-Schönfelder, C., Korn, M., & Shiomi, K. (2009). Sudden drop of seismic velocity after the 2004 M_w 6.6 mid-Niigata earthquake, Japan, observed with Passive Image Interferometry. *Journal of Geophysical Research*, *114*, B06305. https://doi.org/10.1029/2008JB005869

Wegler, U., & Sens-Schönfelder, C. (2007). Fault zone monitoring with passive image interferometry. *Geophysical Journal International*, *168*(3), 1029–1033. https://doi.org/10.1111/j.1365-246X.2006.03284.x

Xia, J., Miller, R. D., & Park, C. B. (1999). Estimation of near surface shear-wave velocity by inversion of Rayleigh waves. *GEOPHYSICS*, *64*, 691–700. https://doi.org/10.1190/1.1444578

Yamagiwa, S., Miyazaki, S., Hirahara, K., & Fukahata, Y. (2015). Afterslip and viscoelastic relaxation following the 2011 Tohoku-oki earthquake (M_w9.0) inferred from inland GPS and seafloor GPS/Acoustic data. *Geophysical Research Letters*, *42*, 66–73. https://doi.org/10.1002/2014GL061735